Electronic supplementary information

Cotton cloth supported tungsten carbide/carbon nanocomposites as a Janus film for solar driven interfacial water evaporation

Bojing Sun[a], Yun Han[a], Siwei Li[a,*], Ping Xu[a], Xijiang Han[a], Ayman Nafady[c], Shengqian Ma[b,*], and Yunchen Du[a,*]

[a] *MIIT Key Laboratory of Critical Materials Technology for New Energy Conversion and Storage, School of Chemistry and Chemical Engineering, Harbin Institute of Technology, Harbin 150001, China*

[b] *Department of Chemistry, University of North Texas, 1508 W Mulberry St, Denton, TX 76201, USA*

[c] *Department of Chemistry, College of Science, King Saud University, Riyadh 11451, Saudi Arabia*

* Corresponding authors.

Tel.: +86-(451)-86413702.

Fax: +86-(451)-86418750.

E-mail address: yunchendu@hit.edu.cn. (Y. Du); Shengqian.Ma@unt.edu (S. Ma); swli@hit.edu.cn (S. Li).

Experimental Section

Preparation of tungsten carbide/carbon nanocomposites

Firstly, 1.0 g of dicyandiamine (DCA) and a required amount of ammonium metatungstate (AMT) were thoroughly ground in an agate motar for 20 mins. The resultant solid mixture was then pyrolyzed at 400 ^{o}C for 0.5 h, then kept at 800 ^{o}C for 5 h under N_2 atmosphere, and the flow rate of N_2 was controlled at 2.5 mL/min. The heating rates from room temperature to 400 ºC and from 400 ºC to 800 ºC were 2 ºC/min and 5 ºC/min, respectivley. The products were denoted as WC/C-*n* in sequence with the weight ratio of AMT to DCA ranging from 0.3 to 5.0. WC/C-1, WC/C-2, WC/C-3 and WC/C-4 correspond to 1:0.3, 1:1, 1:3 and 1:5 of the weight ratio of AMT to DCA, respectively.

Preparation of Janus film with carbide/carbon nanocomposites and cotton cloth

In a typical recipe, 50 mg of WC/C-*n* was dispersed in 0.5 mL of DMF by ultrasonication for 1 hour and stirring for 1 hour to make an aqueous dispersion. Then 15 mg of PVDF was added to the solution and stirred vigorously at room temperature overnight. Finally, a cotton cloth with the area of about 7 cm^2 was spread on a heating plate with 70 ^{o}C, and then the mixed solution was evenly brushed with a brush on the surface of cotton cloth. The resultant Janus film was further denoted as JF-*n*, where *n* referred to the sample of WC/C-*n* in corresponding film.

Characterization

X-ray diffraction (XRD) data were obtained by a Rigaku D/MAXRC X-ray diffractometer (45.0 kV, 50.0 mA) using Cu Kα source. X-ray photoelectron spectroscopy (XPS, Kratos, ULTRA AXIS DLD) was recorded to study the surface states with monochrome Al Kα (hv=1486.6 eV) radiation. Transmission electron microscopy (TEM) images were obtained on a Tecnai F20 instrument operating at an

accelerating voltage of 200 kV. The thermogravimetric analysis was carried out on a SDT Q600 thermogravimetric analyzer (TGA) in the temperature range of room temperature to 800 °C at a heating rate of 10 °C/min under air atmosphere. UV-vis diffuse reflectance spectra were achieved useing a UV-vis spectrophotometer (Lambda 950 (PerkinElmer, USA)) in the range of 200-2500 nm. Metal concentration was made with an Optima 8300 (PerkinElmer, USA) ICP-OES. Total organic carbon (TOC) was determined by Analytik Jena AG MultiN/C 2100 TOC analyzer. The water contact angle was measured by a Goniometer instrument equipped (JC 2000C, ZhongChen, China). A thermal infrared imager (Fotric 225s, China) was used to measure the temperature changes and distributions under light illumination.

Solar-driven water evaporation experiments

The solar-driven water evaporation rate and the solar thermal conversion efficiency were evaluated by the following experiments. All solar-driven water evaporation experiments were conducted by using a solar simulator (CEL-PE300L) with an AM 1.5 filter. A homemade vessel with a surface area of 7.1 cm^2 was used as the evaporation device. A certain amount of 3.5 wt% NaCl solution was added into the vessel. Then, JF-*n* was added into the vessel on the saline water surface. Afterwards, the whole vessel was placed on an analytical electronic balance connected with a computer and illuminated by a light source as mentioned above. An infrared camera was used to measure the surface temperature of JF-*n*. For the cyclic evaporation tests, the test time of each cycle was 1 h, JF-3 was washed with water and vacuum dried after each test, and then used for the next cycle of evaporation. The solar energy efficiency (η) for the solar water evaporation can be calculated according to the following equation:

$$\eta = mh_{LV}/C_{opt}P_0 \quad (1)$$

where m is the steady-state water evaporation rate (kg m^{-2} h^{-1}), h_{LV} is the latent enthalpy of vaporization (kJ kg^{-1}) of the liquid-vapor phase change, C_{opt} is the optical

concentration and P_0 is the solar optical power of one sun (1 kW m^{-2}). The value of h_{LV} varies with temperature. In our experiments, due to the narrow temperature range and the evaporation through large inter-particle voids, the value of h_{LV} only varies very slightly with temperature and thus a constant value of 2260 kJ kg^{-1} is adopted for the calculation.

First-Principles Calculation

DFT calculation was carried out with General Gradient Approximate (GGA) method using Perdew-Burke-Ernzerhof (PBE) exchange-correlation function for geometry optimizations and self-consistent total energy calculation. Calculation was performed with Cambridge Sequential Total Energy Package (CASTEP); the cut-off voltage of plane wave is set at 700 eV, and the total energy convergence at 10^{-6} eV for the self-consistent iterations. Gaussian smearing method with σ=0.05 eV was considered for Brillouin-zone integrations on a 1×1×1 k-mesh. The geometry optimization was performed using a damped molecular dynamics scheme until the forces on the atoms were <0.01 eV/Å. To calculate the phonon spectrum and energy band, the direction of energy was manually selected in Brillouin zone. The setting method was that when calculating the band structure, one should select K points firstly, and different K points corresponded to different convergence accuracy.

Finite Difference Time Domain Simulation (FDTD simulation)

Finite Difference Time Domain Method (implemented on Lumerical ‘‘FDTD Solutions” software package) was utilized for modeling of tungsten carbide nanoparticles (Fig. S12). The diameters of nanoparticles were normalized to the size which was close to that from TEM images. TE polarized plane wave was defined over three-dimensional nanoparticles. For plane wave simulation, a periodic boundary condition was applied in the x and y axial direction, and domains to the side of the clusters were surrounded by water and perfectly matched layers (PMLs). Parameters of tungsten carbide were as follows: the type was Debye-Drude, conductivity was

126,000 S m^{-1}，infinite Freq. relativepermittivity was 5.5, static relative permittivity was 5.5, and density was 17.121 g cm^{-3} from standard PDF card.

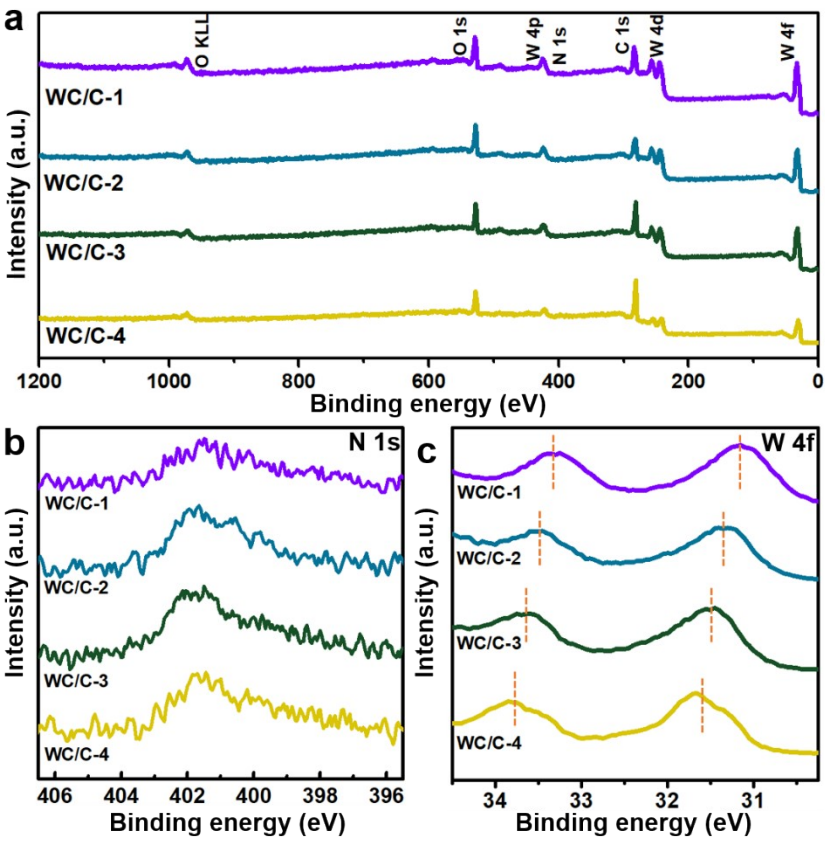

Fig. S1. XPS spectra of full survey (a), N 1s (b), and W 4f (c) of WC/C-*n*.

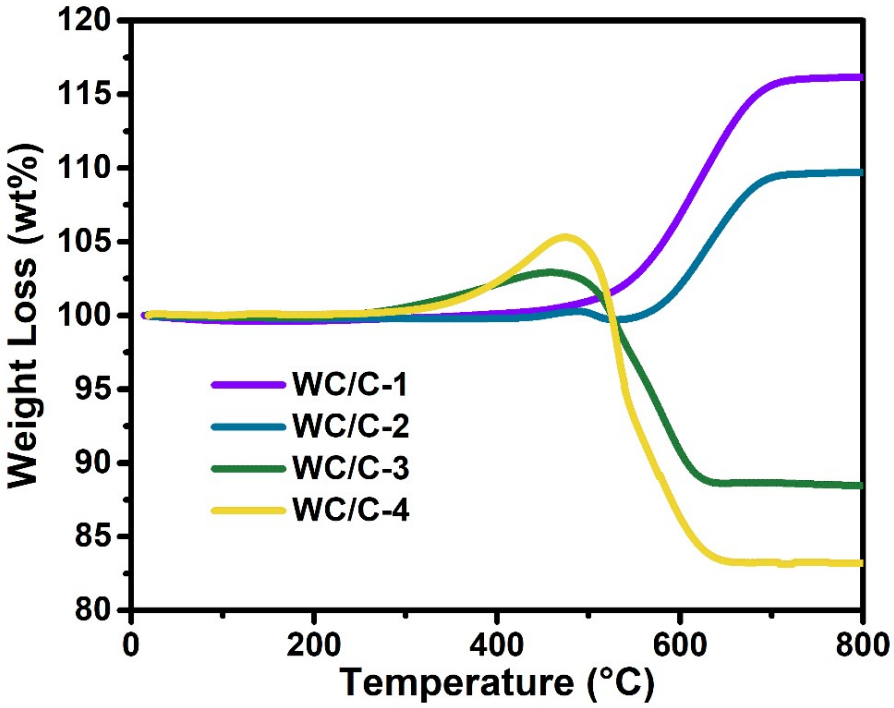

Fig. S2. TG curves of WC/C-*n* under air atmosphere.

WC/C-1 and WC/C-2 are stable before 400 ºC and display obvious weight increases in the temperature of 400-700 ºC. The weight increase should be attributed to the oxidation of WC particles at high temperature. Although carbon combustion is a weight-loss step, these two samples still gain a certain of weight after TG measurements, indicating that their contents of carbon nanosheets are relatively low. In contrast, WC/C-3 and WC/C-4 show similar weight increases in the temperature range of 300-500 ºC, while their total weights drastically decrease after the test. WC/C-3 and WC/C-4 have smaller WC nanoparticles, and thus their onsets for weight increase shift to lower temperature. Meanwhile, their high contents of carbon nanosheets can offset the oxidation of WC nanoparticles. Considering that the final oxidation product of WC nanoparticles is WO_3, one can estimate the specific content of carbon nanosheets with equation:

$$R\ wt\% = (1 - C\ wt\%)\frac{M_{WO_3}}{M_{WC}} \quad (2)$$

where R wt%, C wt%, M_{WO3}, and M_{WC} are referred to remaining weight percentage, carbon nanosheets content, WO_3 formula weight, and WC formula weight, respectively. The calculation results suggest that the specific contents of carbon in WC/C-1, WC/C-2, WC/C-3, and WC/C-4 are 1.9%, 7.2%, 26.5%, and 32.1%, respectively.

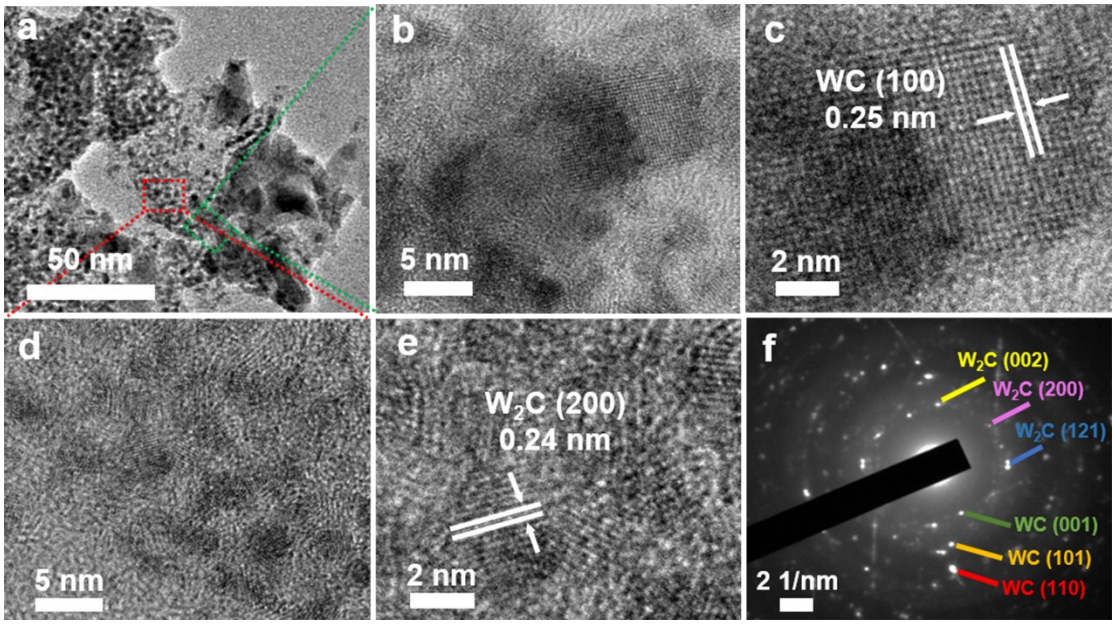

Fig. S3. TEM (a), HR-TEM (b-e) images, and SAED pattern (f) of WC/C-1.

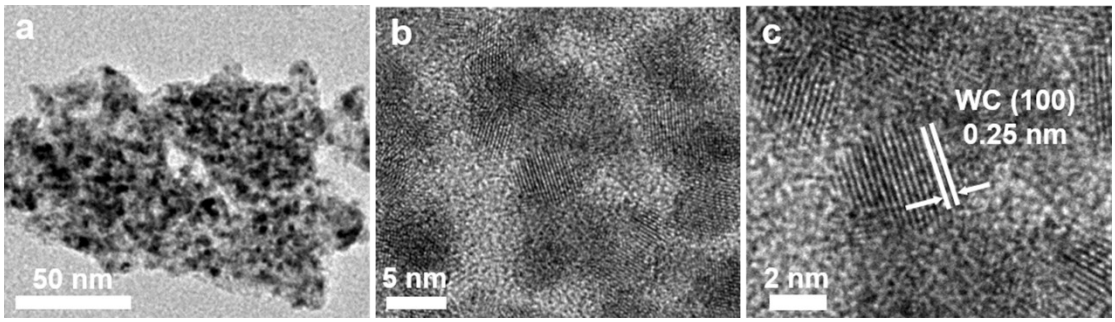

Fig. S4. TEM (a) and HR-TEM (b and c) images of WC/C-2.

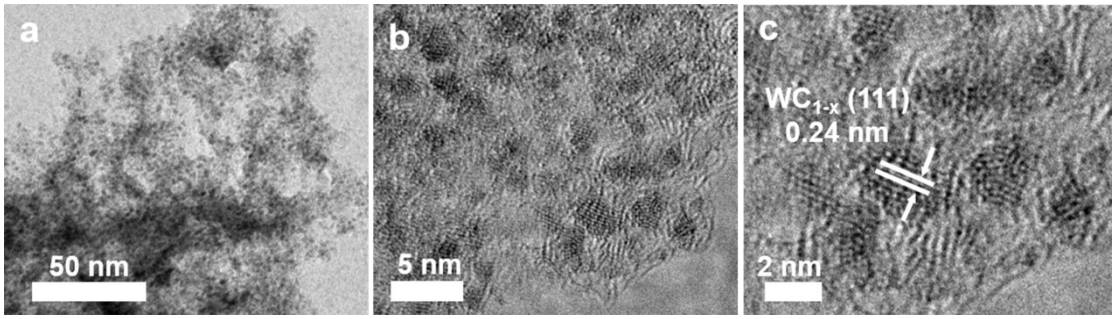

Fig. S5. TEM (a) and HR-TEM (b and c) images of WC/C-4.

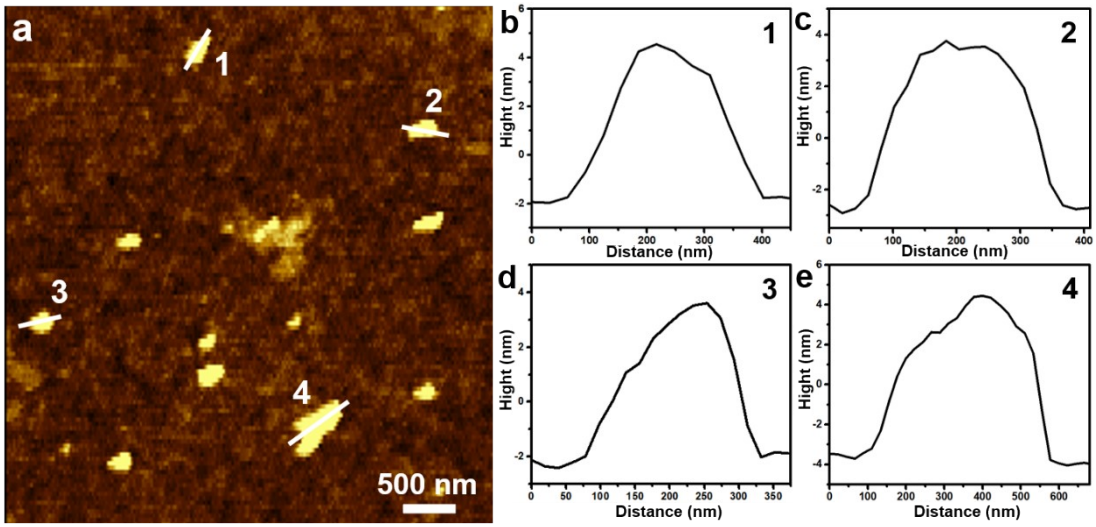

Fig. S6. AFM image (a) and the corresponding height profiles (b-e) of WC/C-3.

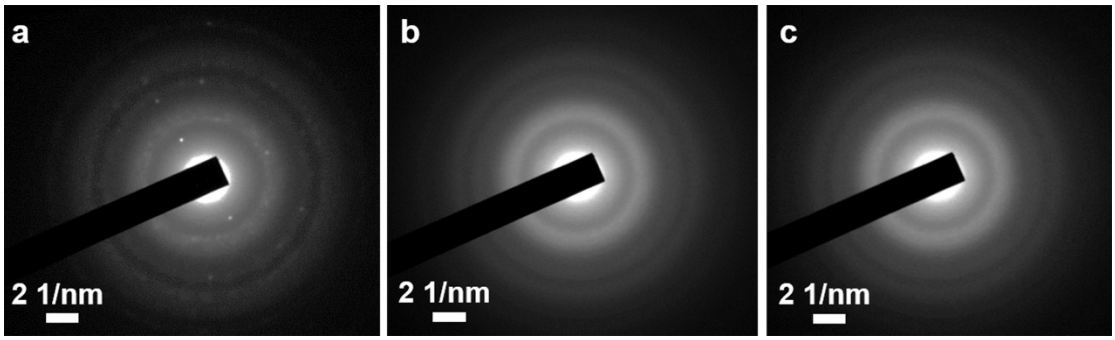

Fig. S7. SAED patterns of WC/C-2 (a), WC/C-3 (b), and WC/C-4 (c).

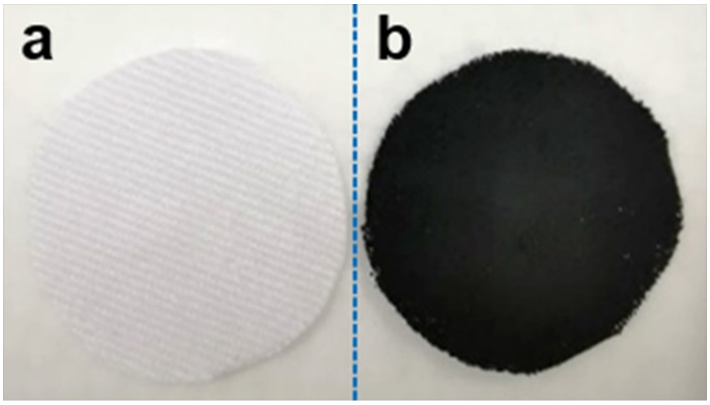

Fig. S8. Optical images of pristine cotton cloth (a) and JF-3 (b).

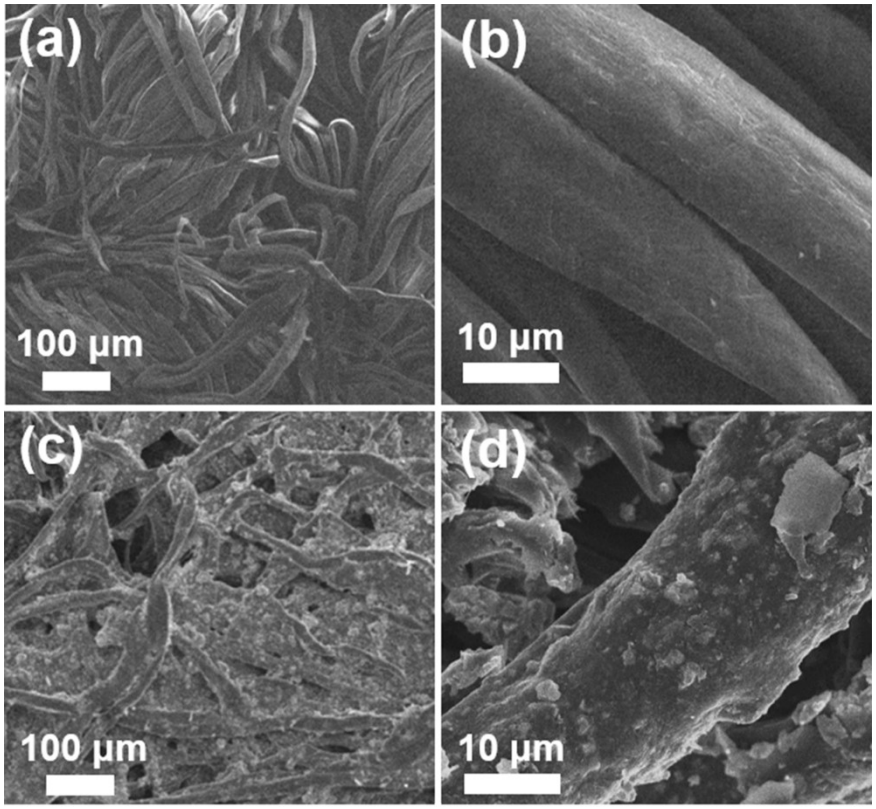

Fig. S9. SEM images of pristine cotton cloth (a and b) and JF-3 (c and d).

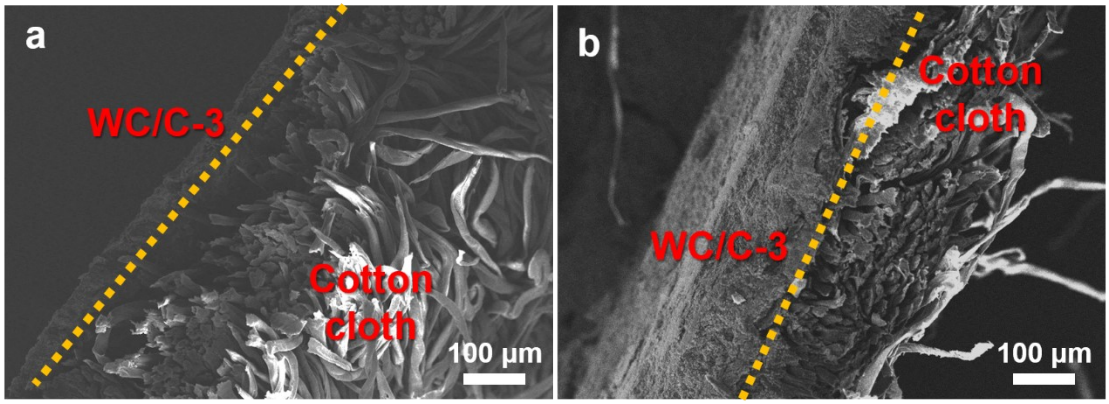

Fig. S10. SEM image of the cross section of JF-3 with different load amount (a: 2.5 mg cm-2; b: 7.0 mg cm-2).

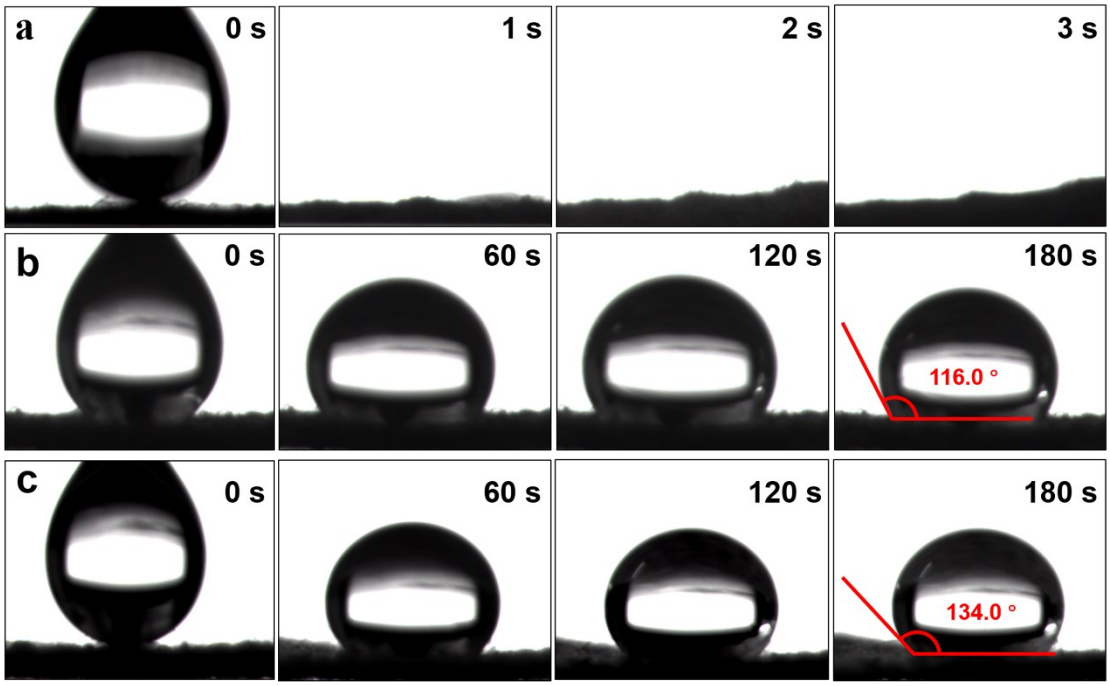

Fig. S11. Camera photos of water droplet impregnation process on the prisitine surface (a), PVDF coating surface (b), and WC/C-3 coating surface (c) of JF-3.

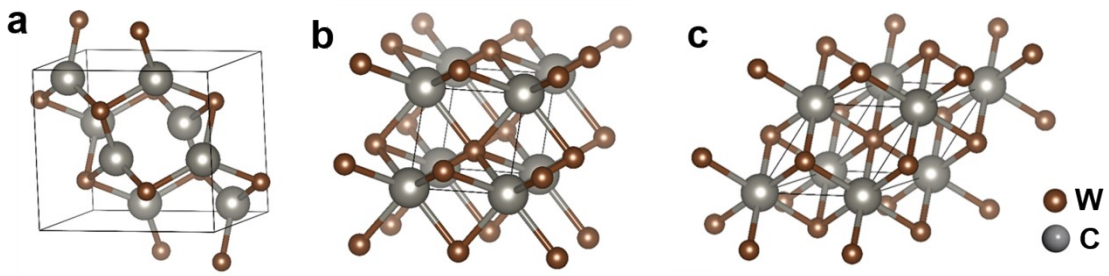

Fig. S12. Crystal structure models of W_2C (a), WC (b), and WC_{1-x} (c).

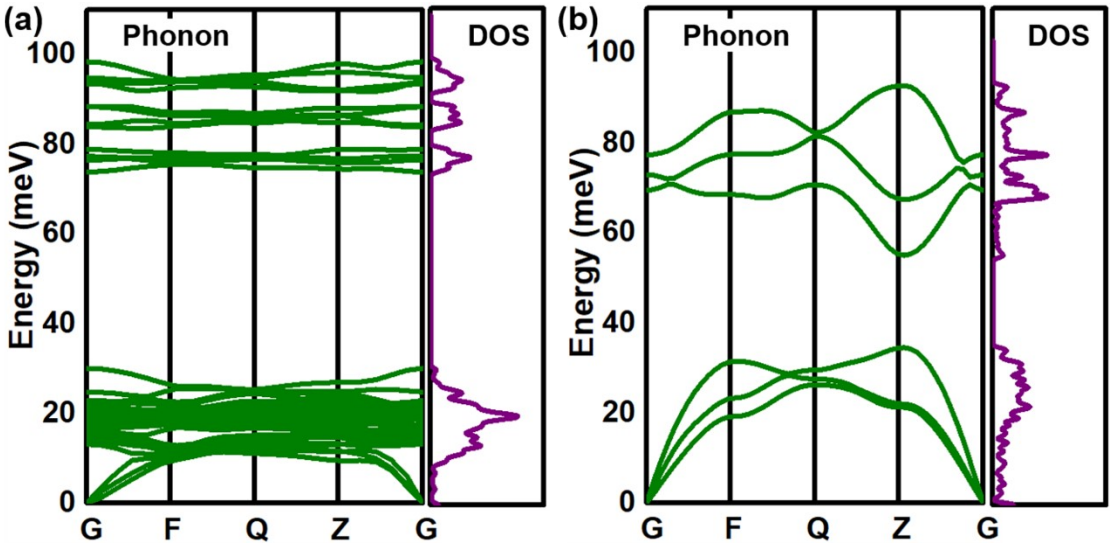

Fig. S13. Phonon band structure and density of states of W_2C (a) and WC (b).

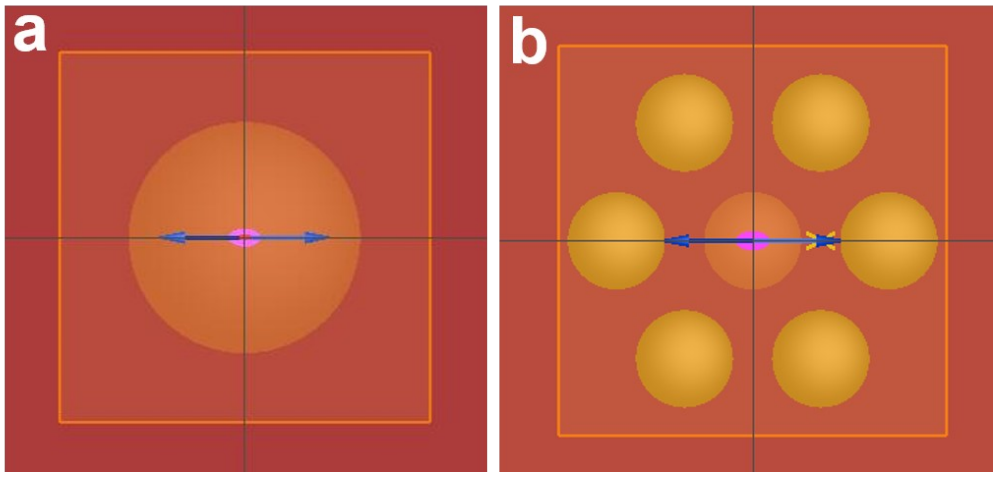

Fig. S14. Models for FDTD simulation of single WCNP with a diameter of 50 nm (a), and a group of WCNPs with average diameter of 5 nm (b).

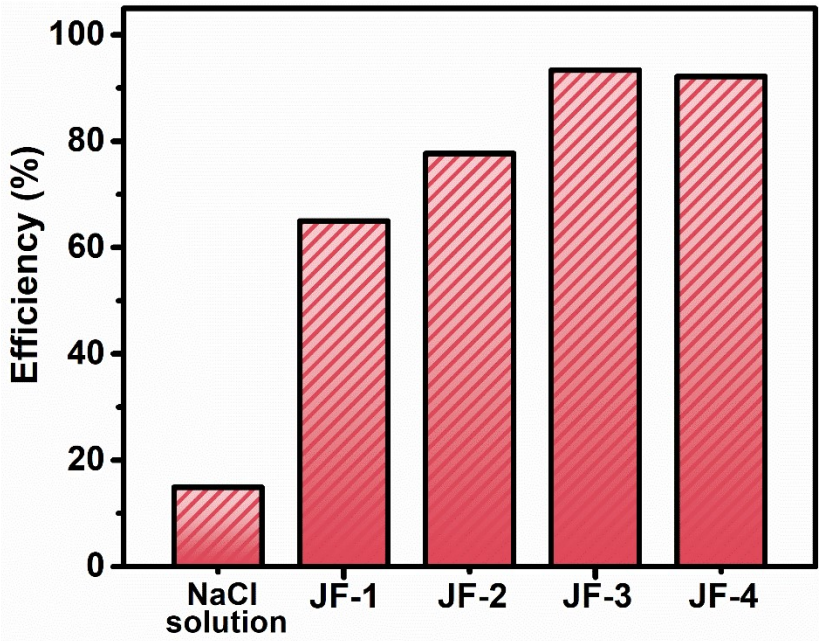

Fig. S15. Solar-to-water conversion efficiencies of 3.5 wt% NaCl solution without and with the aid of Janus evaporation film.

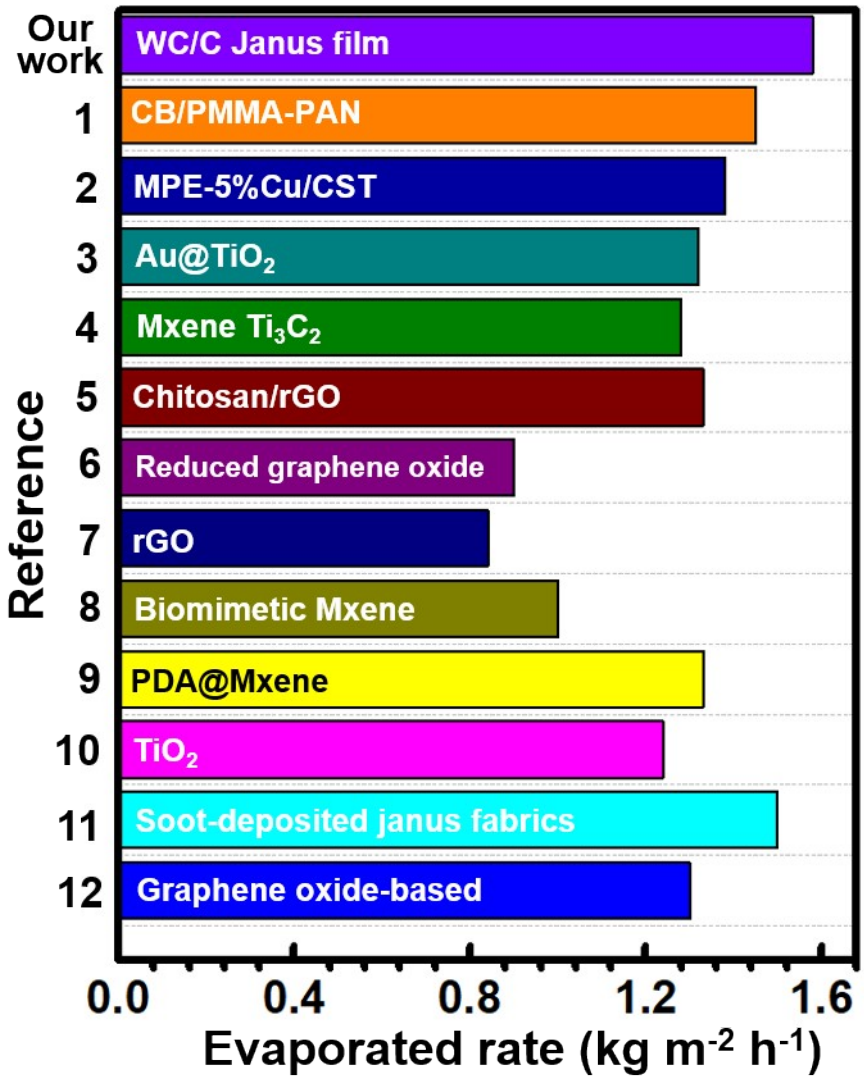

Fig. S16. Water evaporation performance of evaporation films ever published (under AM1.5 irradiation).

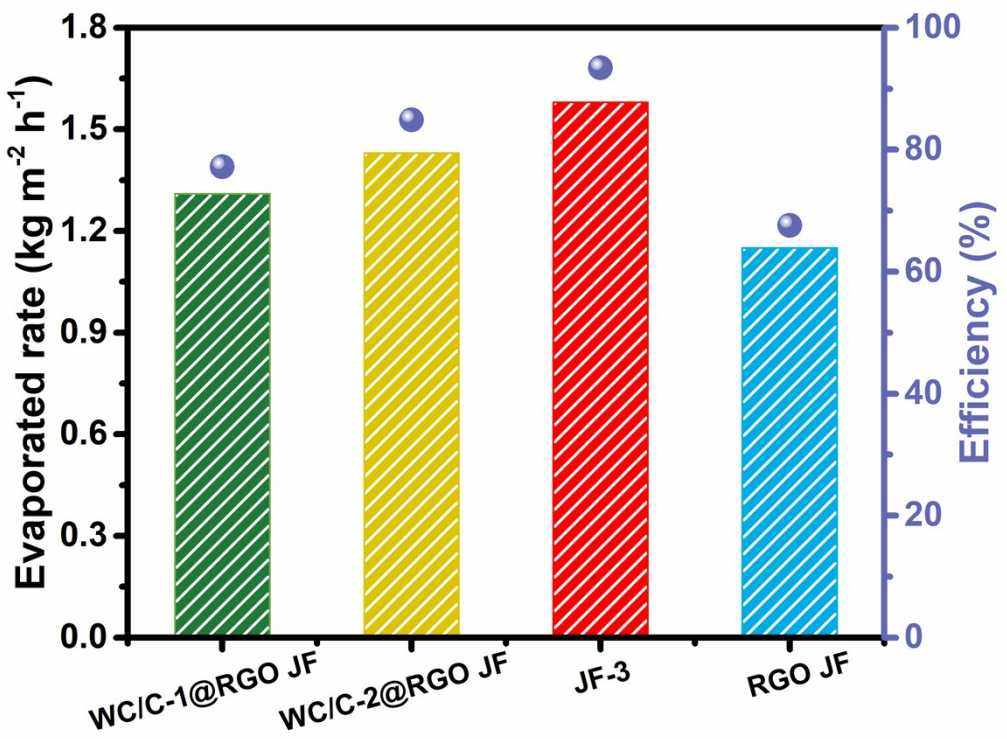

Fig. S17. Water evaporation rates and photothermal conversion efficiencies of WC/C-1@RGO JF, WC/C-2@RGO JF, JF-3, and RGO JF.

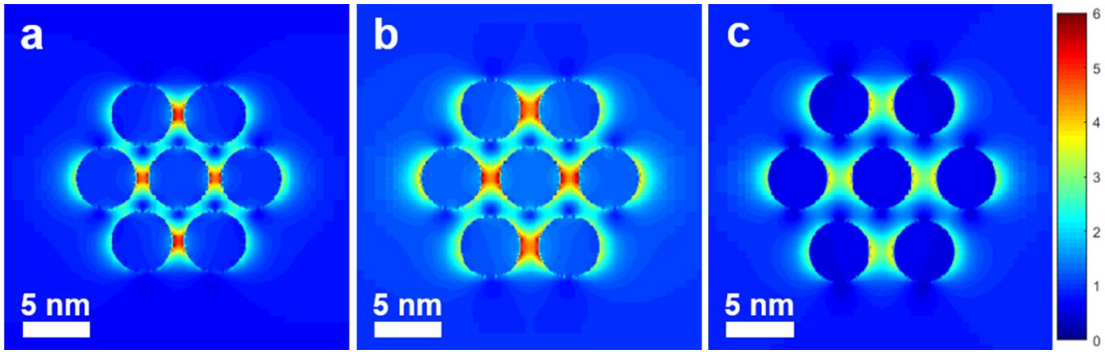

Fig. S18. Electric field distribution of WCNPs with inner-particle distance of 1 nm (a), 1.5 nm (b) and 2 nm (c) under 550 nm light input.

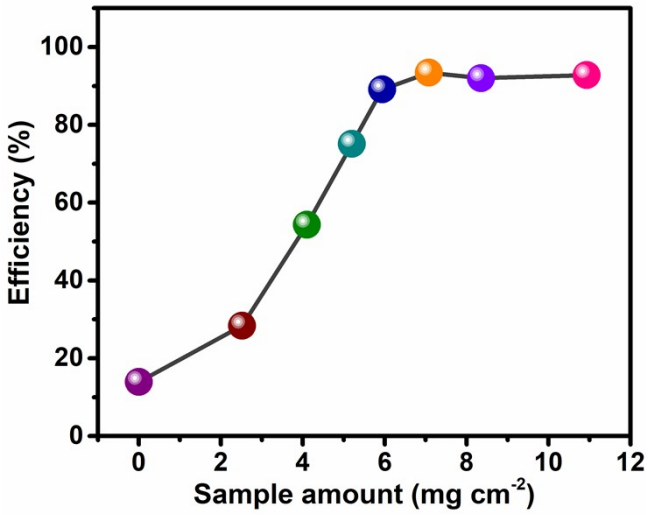

Fig. S19. Load-dependent photothermal conversion efficiencies of JF-3. All solar-to-water efficiencies are calculated by subtracting the natural seawater evaporation efficiency in dark.

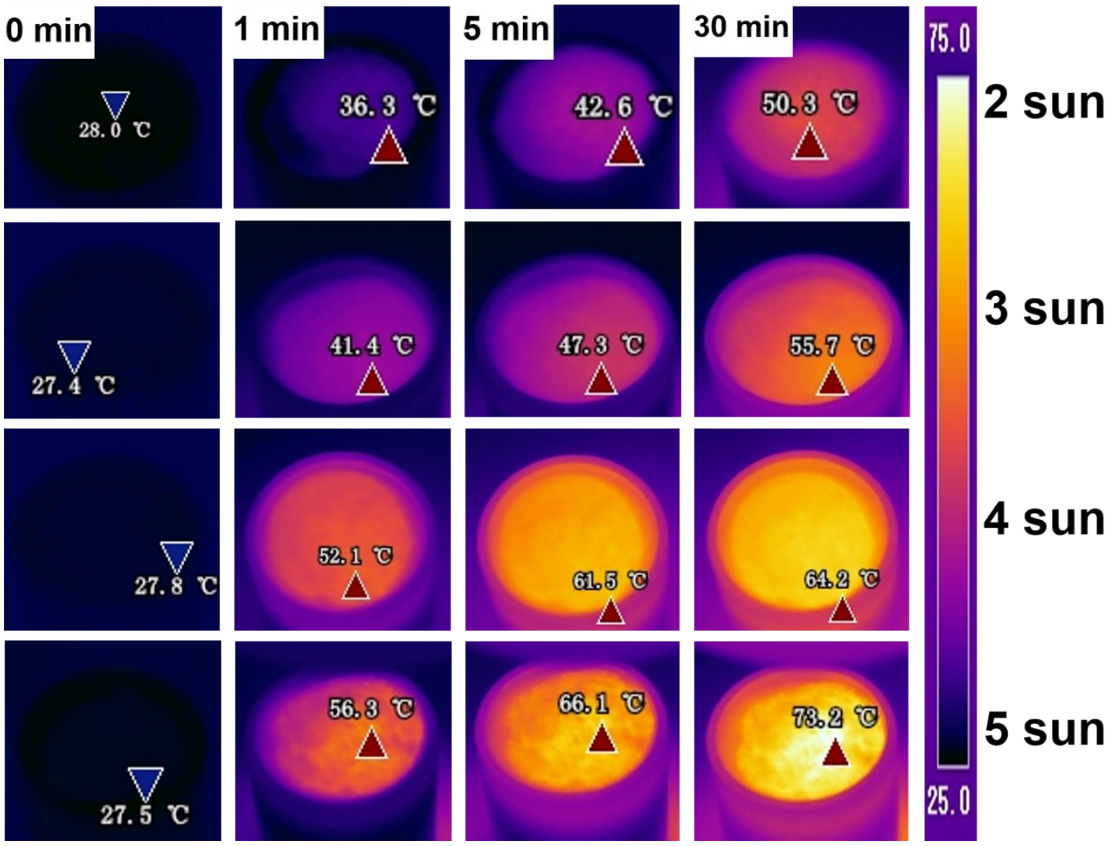

Fig. S20. IR images of JF-3 under different irradiation powers.

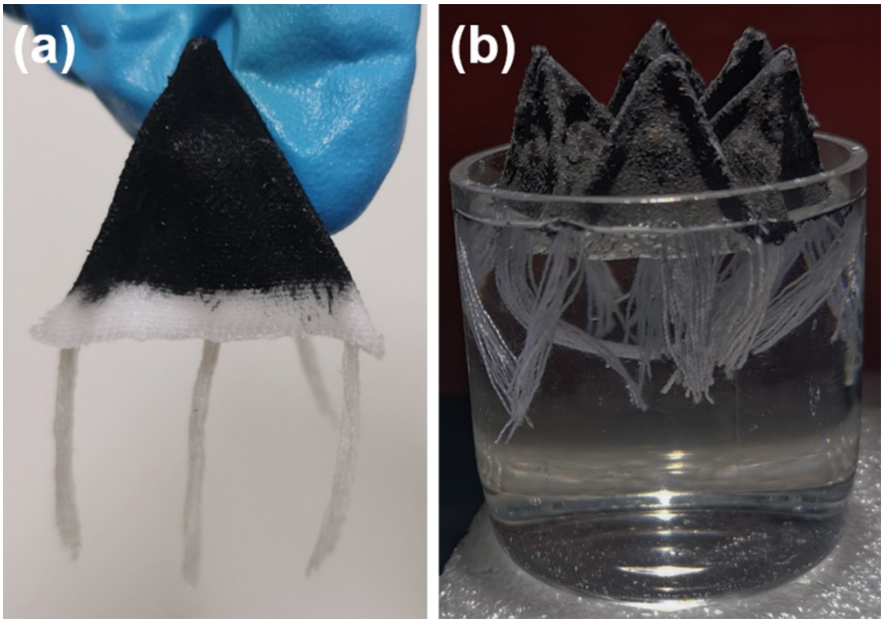

Fig. S21. Optical images of single pyramidal evaporator (a) and pyramid-array evaporator (b).

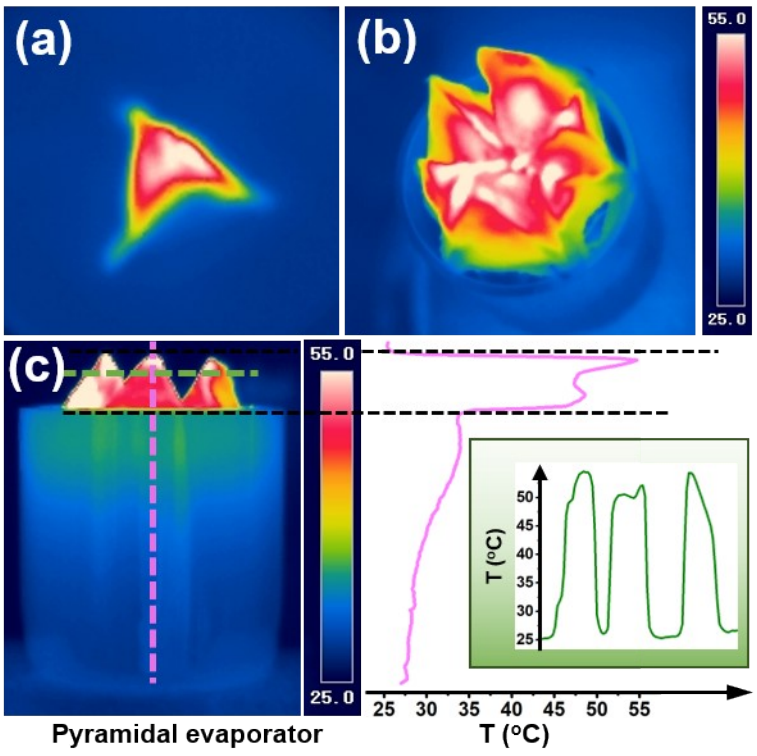

Fig. S22. IR images of top surface for single pyramidal evaporator (a) and pyramid-array evaporator (b). IR images of side face and temperature profiles of water-air interface without and with pyramidal evaporator under light irradiation for 30 min (c).

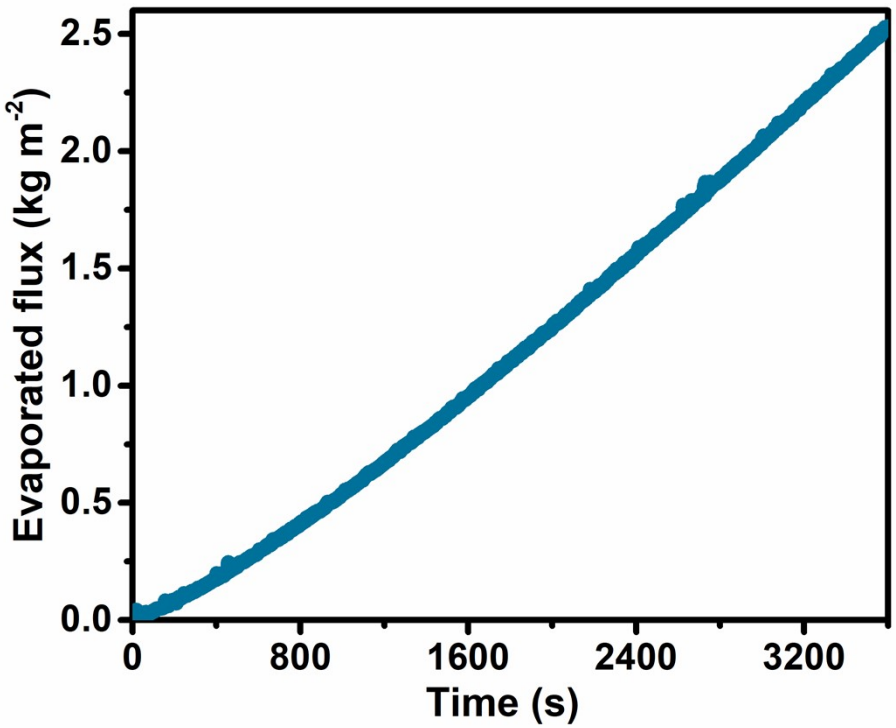

Fig. S23. Water evaporation flux evolution of 3.5 wt% NaCl saline water with the aid of pyramidal evaporator.

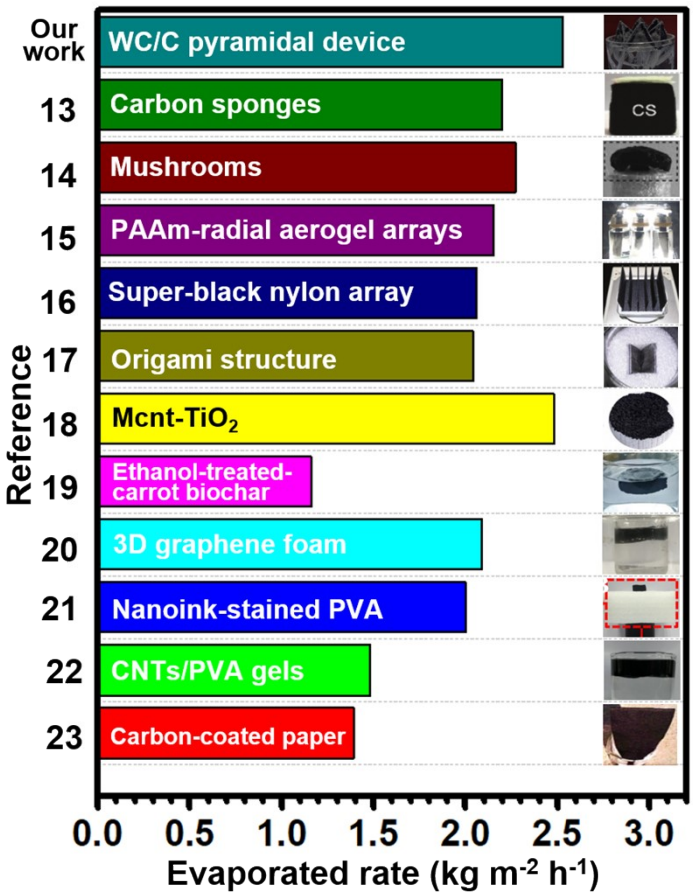

Fig. S24. Water evaporation performance of evaporators with different configurations reported recently (under AM1.5 irradiation).

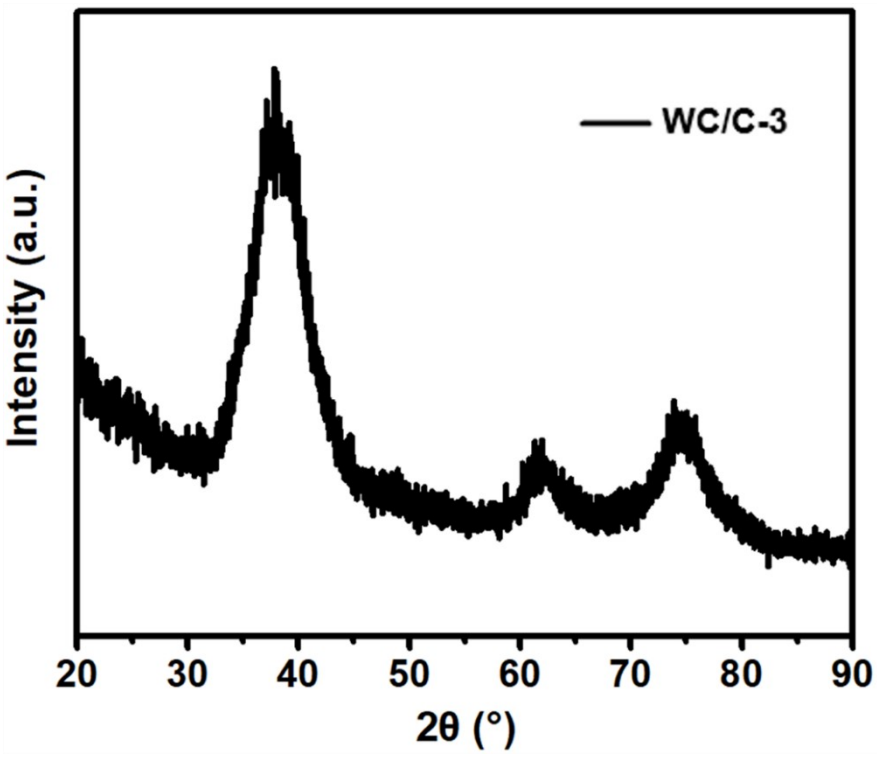

Fig. S25. XRD pattern of WC/C-3 after ten hours illumination.

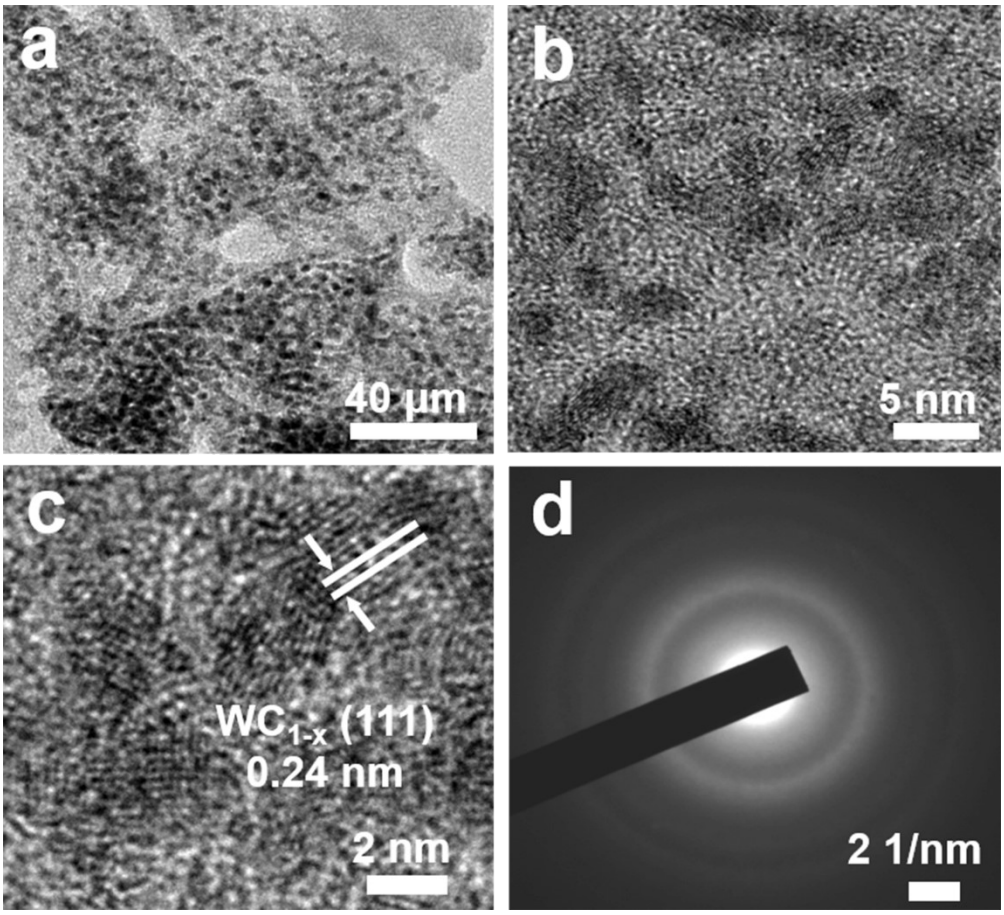

Fig. S26. TEM (a), HR-TEM (b and c) images, and SAED pattern (d) of WC/C-3 after ten hours illumination.

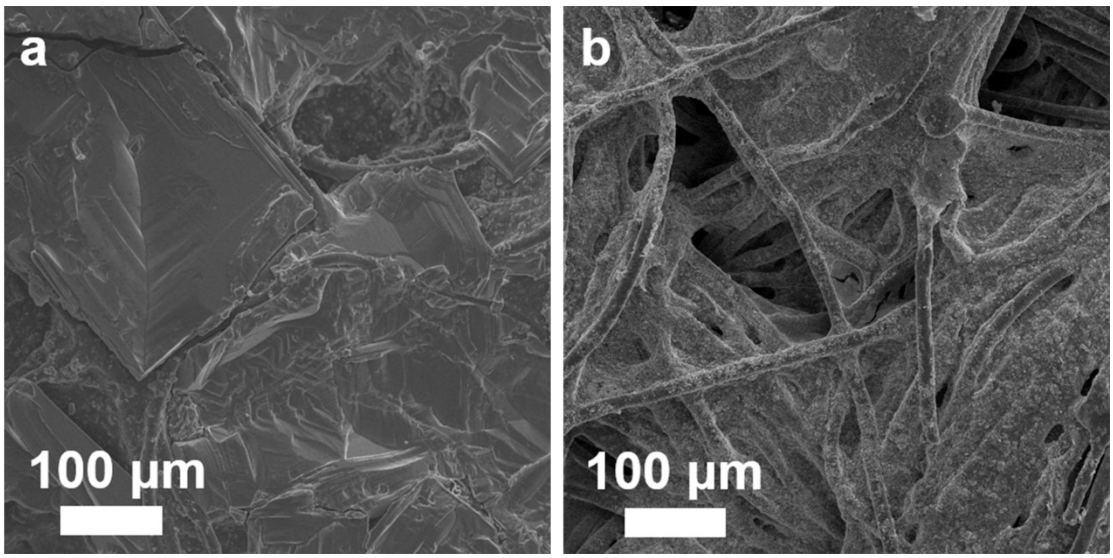

Fig. S27. SEM images of surface of JF-3 after 4 hours of illumination (a) and 2 hours after turning off the lights (b).

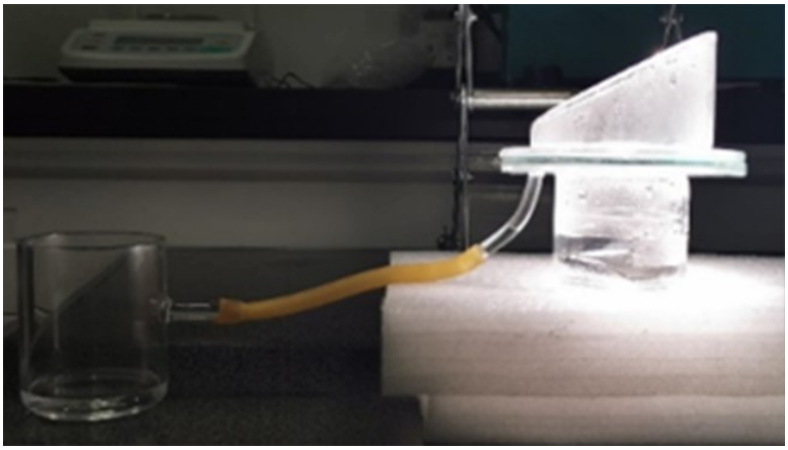

Fig. S28. Optical image of solar-driven water evaporation and the liquid water collection device.

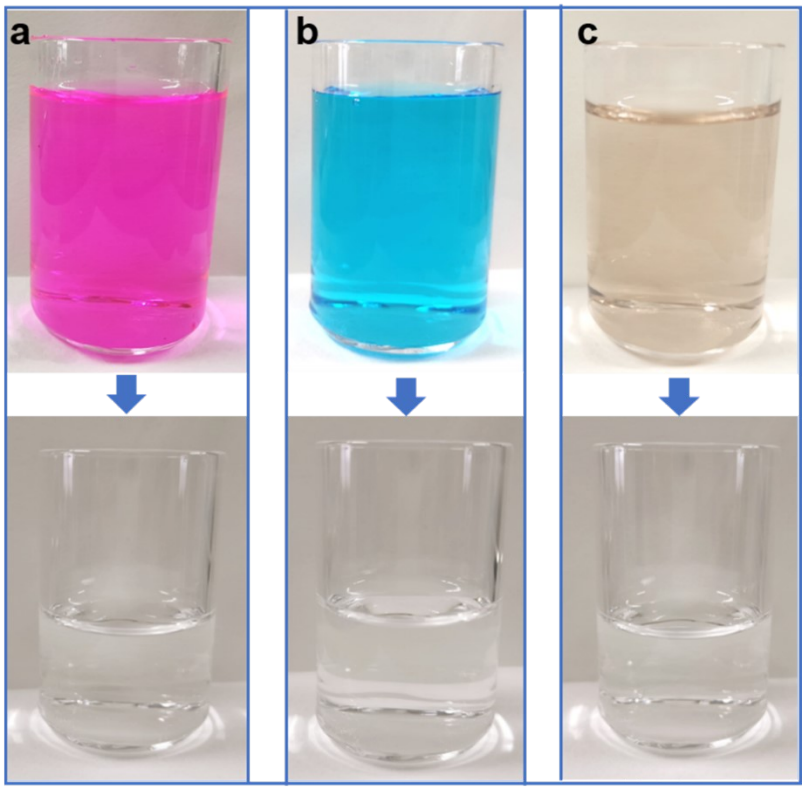

Fig. S29. Comparison of photos of RhB (a), MB (b), and Tetracycline (c) before and after evaporation.

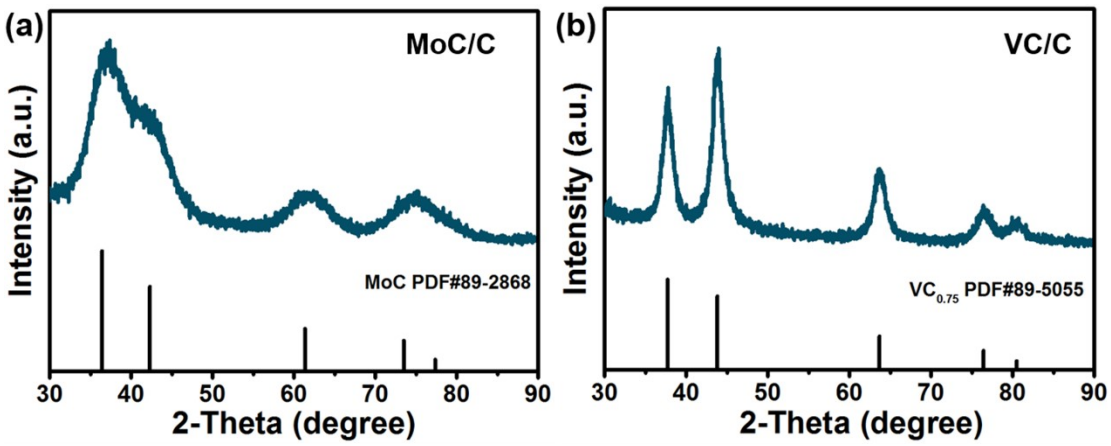

Fig. S30. XRD patterns of MoC/C (a) and VC/C (b).

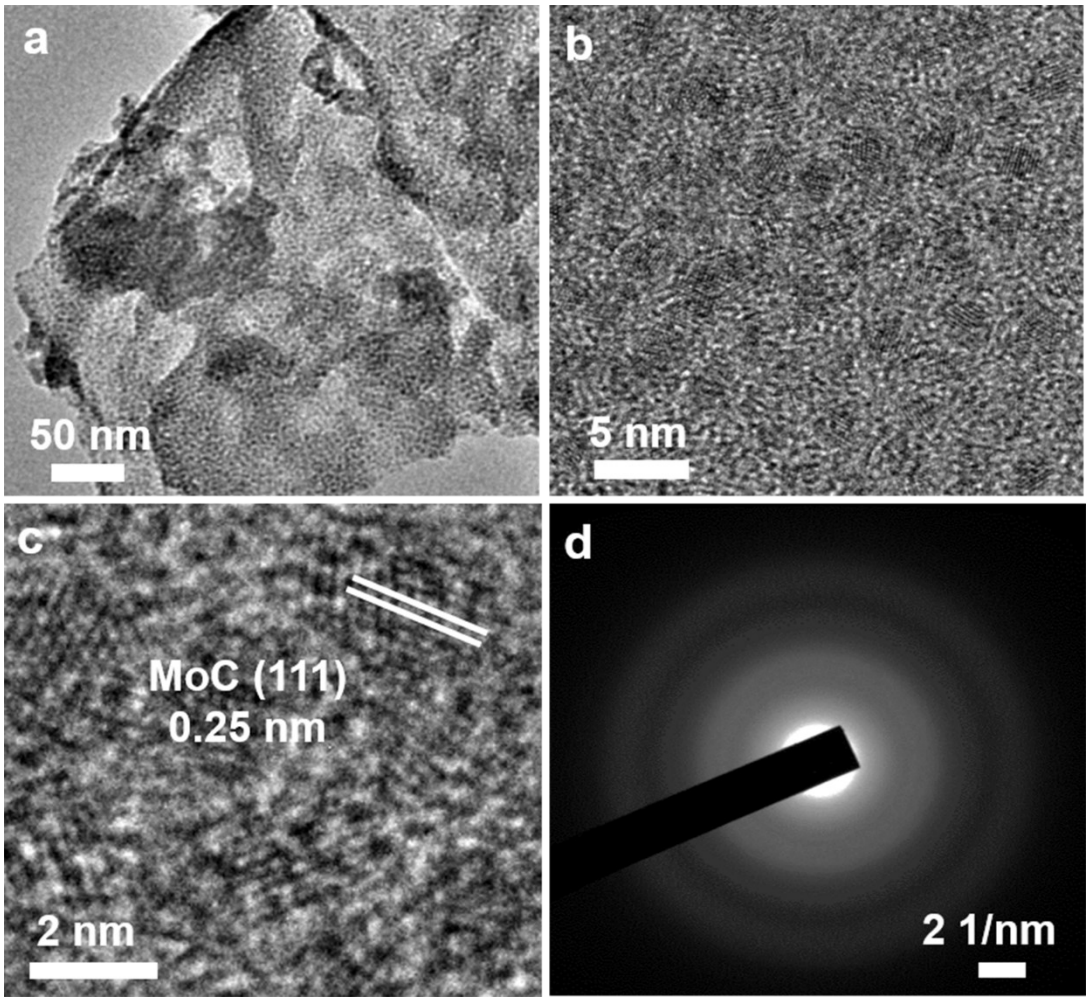

Fig. S31. TEM (a) and HRTEM (b and c) images, and SAED pattern (d) of MoC/C.

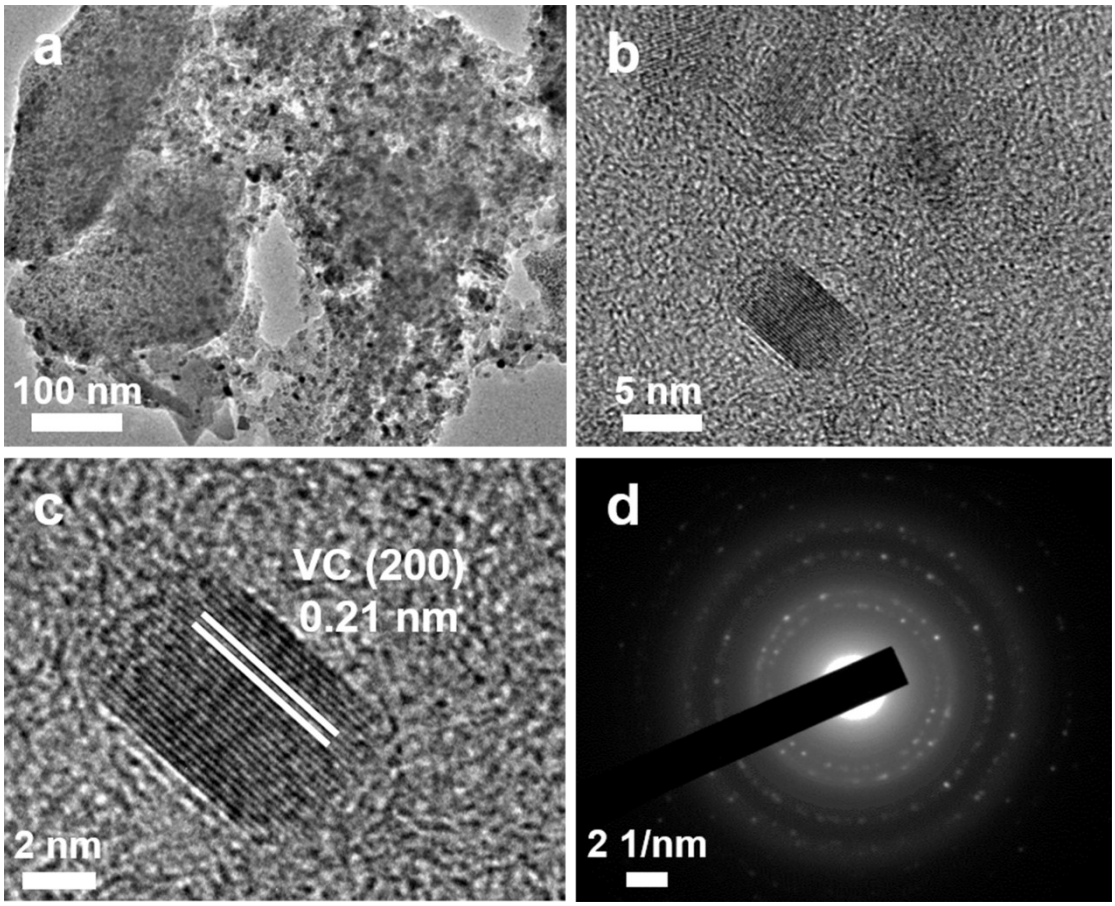

Fig. S32. TEM (a), HR-TEM (b, c) images, and SAED pattern (d) of VC/C.

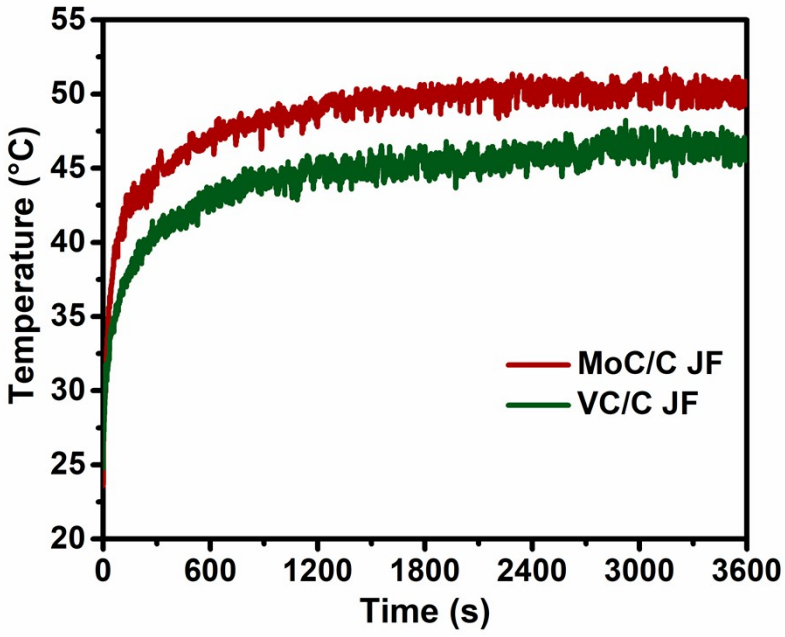

Fig. S33. Surface temperature changes of MoC/C and VC/C Janus films.

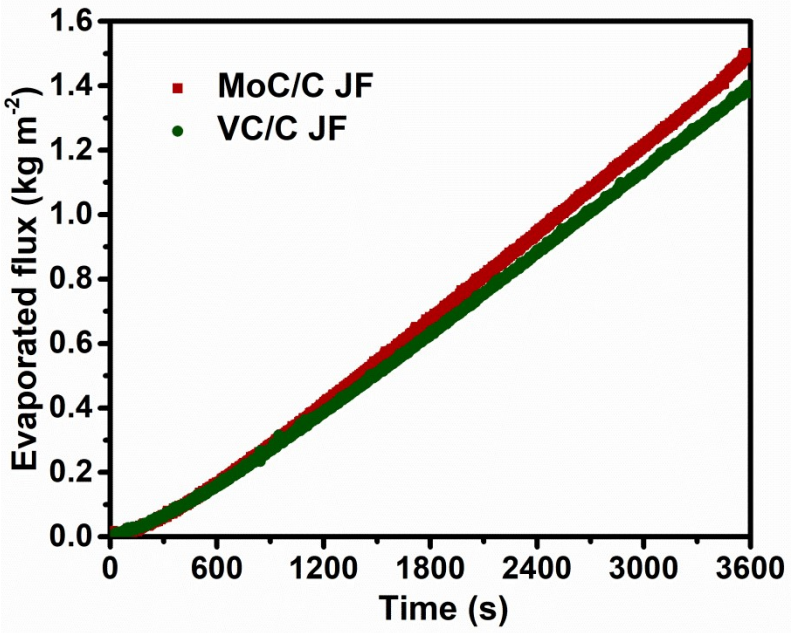

Fig. S34. Water evaporation flux evolution of MoC/C and VC/C Janus films.

References

[1] Xu WC, Hu XZ, Zhuang SD, et al. Flexible and salt resistant Janus absorbers by electrospinning for stable and efficient solar desalination. Adv Energy Mater 2018, 8: 1702884.

[2] Zhang XC, Wang XN, Wu WD, et al. Self-floating monodisperse microparticles with a nano-engineered surface composition and structure for highly efficient solar-driven water evaporation. J Mater Chem A, 2019, 7: 6963–71.

[3] Huang J, He YR, Chen MJ, et al. Solar evaporation enhancement by a compound film based on Au@TiO_2 core–shell nanoparticles, Sol Energy 2017, 155: 1225-32.

[4] Li RY, Zhang LB, Shi L, et al. MXene Ti_3C_2: an effective 2D light-to-heat conversion material. ACS Nano 2017, 11: 3752-9.

[5] Wang F, Wei DY, Li YZ, et al. Chitosan/reduced graphene oxide-modified spacer fabric as a salt-resistant solar absorber for efficient solar steam generation. J Mater Chem A 2019, 7: 18311-7.

[6] Wang G, Fu Y, Ma XF, et al. Reusable reduced graphene oxide based double-layer system modified by polyethylenimine for solar steam generation. Carbon 2017, 114: 117-24.

[7] Cheng G, Wang XZ, Liu X, et al. Enhanced interfacial solar steam generation with composite reduced graphene oxide membrane Sol Energy 2019, 194: 415-30.

[8] Li KR, Chang TH, Li ZP, et al. Biomimetic MXene textures with enhanced light-to-heat conversion for solar steam generation and wearable thermal management. Adv Energy Mater 2019, 9: 1901687.

[9] Zhao X, Zha XJ, Tang LS, et al. Self-assembled core-shell polydopamine@MXene with synergistic solar absorption capability for highly efficient solar-to-vapor generation. Nano Res 2020, 13: 255-64.

[10] Wang J, Li YY, Deng L, et al. High-performance photothermal conversion of narrow-bandgap Ti_2O_3 nanoparticles. Adv Mater 2017, 29: 1603730.

[11] Gao SW, Dong XL, Huang JY, et al. Bioinspired soot-deposited Janus fabrics for sustainable solar steam generation with salt-rejection. Glob Chall 2019, 3: 1800117.

[12] Li XQ, Xu WC, Tang MY, et al. Graphene oxide-based efficient and scalable solar desalination under one sun with a confined 2D water path. PNAS 2016, 113: 13953-8.

[13] Zhu LL, Gao MM, Peh CKNP, et al. Self-contained monolithic carbon sponges for solar-driven interfacial water evaporation distillation and electricity generation. Adv Energy Mater 2018, 8: 1702149.

[14] Xu N, Hu XZ, Xu WC, et al. Mushrooms as Efficient Solar Steam-Generation Devices. Adv. Mater. 2017, 29: 1606762.

[15] Xu WZ, Xing Y, Liu J, et al. Efficient water transport and solar steam generation via radially, hierarchically structured aerogels. ACS Nano 2019, 13: 7930-8.

[16] Tu C, Cai WF, Chen X, et al. A 3D-structured sustainable solar-driven steam generator using super-black nylon flocking materials. Small 2019, 15: 1902070.

[17] Xu Y, Ma JX, Liu DQ, et al. Origami system for efficient solar driven distillation in emergency water supply. Che. Eng J 2019, 356: 869-76.

[18] Sun ZZ, Li WZ, Song WL, et al. A high-efficiency solar desalination evaporator composite of corn stalk, Mcnts and TiO_2: ultra-fast capillary water moisture transportation and porous bio-tissue multi-layer filtration. J Mater Chem A 2020, 8: 349-57.

[19] Long YJ, Huang SL, Yi H, et al. Carrot-inspired solar thermal evaporator. J Mater Chem A 2019, 7: 26911-6.

[20] Hu GY, Cao Y, Huang MY, et al. Salt-resistant carbon nanotubes/polyvinyl alcohol hybrid gels with tunable water transport for high-efficiency and long-term solar steam generation. Energy Technol 2020, 8: 1900721.

[21] Yang Y, Zhao RQ, Zhang TF, et al. Graphene-based standalone solar energy converter for water desalination and purification. ACS Nano 2018, 12: 829-35.

[22] Deng ZY, Miao L, Liu PF, et al. Extremely high water-production created by a nanoink-stained PVA evaporator with embossment structure. Nano Energy 2019, 55: 368-76.

[23] Song HM, Liu YH, Liu ZJ, et al. Cold vapor generation beyond the input solar energy limit. Adv Sci 2018, 5: 1800222.